



Enabling real-time detection of electrochemical desorption phenomena with sub-monolayer sensitivity

Trimarco, Daniel Bøndergaard; Scott, Søren Bertelsen; Thilsted, Anil Haraksingh; Pan, Jesper Yue; Pedersen, Thomas; Hansen, Ole; Chorkendorff, Ib; Vesborg, Peter Christian Kjærgaard

Published in:
Electrochimica Acta

Link to article, DOI:
[10.1016/j.electacta.2018.02.060](https://doi.org/10.1016/j.electacta.2018.02.060)

Publication date:
2018

Document Version
Peer reviewed version

[Link back to DTU Orbit](#)

Citation (APA):
Trimarco, D. B., Scott, S. B., Thilsted, A. H., Pan, J. Y., Pedersen, T., Hansen, O., Chorkendorff, I., & Vesborg, P. C. K. (2018). Enabling real-time detection of electrochemical desorption phenomena with sub-monolayer sensitivity. *Electrochimica Acta*, 268, 520-530. <https://doi.org/10.1016/j.electacta.2018.02.060>

General rights

Copyright and moral rights for the publications made accessible in the public portal are retained by the authors and/or other copyright owners and it is a condition of accessing publications that users recognise and abide by the legal requirements associated with these rights.

- Users may download and print one copy of any publication from the public portal for the purpose of private study or research.
- You may not further distribute the material or use it for any profit-making activity or commercial gain
- You may freely distribute the URL identifying the publication in the public portal

If you believe that this document breaches copyright please contact us providing details, and we will remove access to the work immediately and investigate your claim.

Accepted Manuscript

Enabling real-time detection of electrochemical desorption phenomena with sub-monolayer sensitivity

Daniel B. Trimarco, Soren B. Scott, Anil H. Thilsted, Jesper Y. Pan, Thomas Pedersen, Ole Hansen, Ib Chorkendorff, Peter C.K. Vesborg



PII: S0013-4686(18)30343-8

DOI: [10.1016/j.electacta.2018.02.060](https://doi.org/10.1016/j.electacta.2018.02.060)

Reference: EA 31255

To appear in: *Electrochimica Acta*

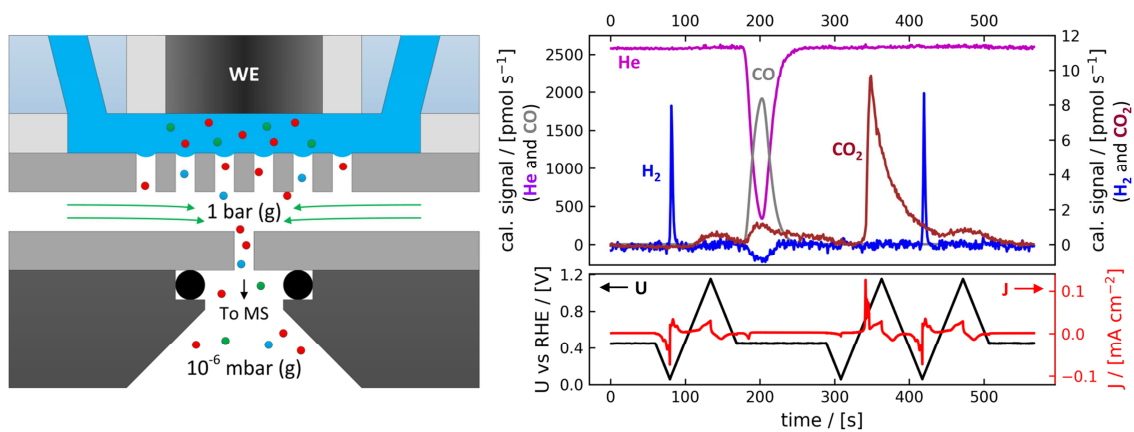
Received Date: 22 December 2017

Revised Date: 6 February 2018

Accepted Date: 12 February 2018

Please cite this article as: D.B. Trimarco, S.B. Scott, A.H. Thilsted, J.Y. Pan, T. Pedersen, O. Hansen, I. Chorkendorff, P.C.K. Vesborg, Enabling real-time detection of electrochemical desorption phenomena with sub-monolayer sensitivity, *Electrochimica Acta* (2018), doi: 10.1016/j.electacta.2018.02.060.

This is a PDF file of an unedited manuscript that has been accepted for publication. As a service to our customers we are providing this early version of the manuscript. The manuscript will undergo copyediting, typesetting, and review of the resulting proof before it is published in its final form. Please note that during the production process errors may be discovered which could affect the content, and all legal disclaimers that apply to the journal pertain.



Enabling real-time detection of electrochemical desorption phenomena with sub-monolayer sensitivity

Daniel B. Trimarco^{a,b,1}, Soren B. Scott^{a,1}, Anil H. Thilsted^b, Jesper Y. Pan^c, Thomas Pedersen^c, Ole Hansen^c, Ib Chorkendorff^a, Peter C. K. Vesborg^{a,*}

^a*Department of Physics, Technical University of Denmark, Fysikvej, Building 312, DK-2800 Kgs. Lyngby, Denmark*

^b*Spectro Inlets ApS, Fysikvej, Building 312, DK-2800 Kgs. Lyngby, Denmark*

^c*Department of Micro- and Nanotechnology, Technical University of Denmark, Ørstedes Plads, Building 344, DK-2800 Kgs. Lyngby, Denmark*

Keywords:

mass spectrometry, DEMS, OLEMS, platinum, electrocatalysis

Abstract

Electrochemical reactions play an increasingly important role in sustainable energy conversion and chemical synthesis. Better understanding of catalytic mechanisms at electrode surfaces is thus important for the transition to a clean-energy economy, but is hindered by the difficulty of real-time detection of reaction products and intermediates during electrochemistry experiments. Herein, we present a new type of electrochemistry – mass spectrometry (EC-MS) based on a versatile gas inlet to vacuum fabricated onto a silicon microchip, and compare it to established techniques with focus on sensitivity, time response, and mass transport. The inlet system is able to capture reactant molecules directly from an electrode surface and pass them on to a mass spectrometer on a sub-second time scale with 100% collection efficiency for quantitative analysis with unprecedented sensitivity. The high sensitivity and fast time-response, coupled with well-characterized mass transport of both reactants and products in this setup enables sub-turnover resolution for analysis of electrochemical reactions. The technology and concepts presented here can serve as a platform to improve in-situ mass spectrometry in electrochemistry as well as other fields.

*Corresponding author

Email address: peter.vesborg@fysik.dtu.dk (Peter C. K. Vesborg)

¹These authors contributed equally

1. Introduction

A transition from fossil fuels to sustainable energy sources like wind and solar and sustainable chemical feedstocks like water, carbon dioxide, and biomass is strictly necessary to avoid catastrophic climate change [1]. This transition is bringing a drastic change in the global energy landscape, causing electrochemical and biochemical processes to play an increasing role [2, 3, 4]. In order to improve the economics of sustainable energy conversion and chemical synthesis, it is thus important to expand fundamental understanding of electrochemical and biochemical processes.

Electrochemical and biochemical processes are generally run in wet environments at or above ambient pressure, while the most versatile tool for identifying and quantifying the reaction products, mass spectrometry, requires high vacuum [5]. A wide range of sample introduction and ionization methods have been developed that are suitable for product identification and quantification by mass spectrometry after a batch reaction [6], but experiments investigating reaction kinetics and catalytic mechanisms in electrochemistry and biochemistry can be greatly facilitated by in-situ and real-time, i.e., second-scale, product detection in a small reaction volume [7, 8]. This underscores the need for fast, sensitive, and quantitative real-time delivery of reaction products from a liquid test environment to high vacuum [9]. As electrochemical experiments using modern instrumentation allow for finely controlled and near-instant experimental input and output in the form of electrode potential and electric current, electrochemistry – mass spectrometry (EC-MS) thus serves as a natural platform for the refining of real-time mass spectrometry methods which can then be adopted in other fields.

Membrane inlet mass spectrometry (MIMS), the earliest technique for studying dissolved analytes with mass spectrometry, which remains widely used in environmental and bio-analytical applications, was also applied to electrochemistry early on [10]. In MIMS, the liquid testing environment is separated from the vacuum of the mass spectrometer by a semipermeable polymer membrane. To protect the vacuum, the membrane must be thick enough to prevent excessive permeation of the solvent, but as the analyte also must diffuse through the membrane, this slows the response time, generally up to several minutes [11]. A much faster response time was later achieved by the use of a porous polytetrafluoroethylene (PTFE) membrane [12], but the correspondingly higher flux of solvent and analyte across the membrane necessitated a differential pumping stage, forming the basis of differential electrochemical mass spectrometry (DEMS), where the term "differential" emphasizes that the mass spectrometer signal represents a snapshot of the analyte concentration at the membrane [13]. DEMS has since been developed extensively, particularly through the work of Helmut Baltruschat and coworkers [14, 15, 16], and has become a widely used method in electrocatalysis research [17, 18, 19, 20]. DEMS has proven especially useful in fundamental electrochemical studies, for example comparing the product distribution of a Faradaic process on different crystal facets [21, 22, 23]. A notable variation on DEMS, termed on-line mass spectrometry (OLEMS), developed by Marc Koper and coworkers [24, 25, 26] and now used by several groups [27, 28], involves a small PTFE vacuum inlet at the end of a glass tube as an EC-MS probe, scaled such that the flux to the mass spectrometer is sufficiently small that no differential pumping is needed.

Much of the development in DEMS the past three decades has focused on the cell that interfaces the electrochemical experiment and the vacuum inlet. In the original DEMS experiments, the working electrode was sputtered onto the PTFE membrane of the vacuum inlet [13], giving the fastest possible time response but complicating construction of the interface and restricting the materials that could be studied. The advent of a

stagnant thin-layer cell [14] made it possible to perform DEMS on smooth electrodes, but effects of solvent evaporation made it difficult to perform experiments in a controlled environment. This was remedied by the advent of a dual thin-layer flow cell in which the working electrode and vacuum inlet are in separate compartments [29]. This dual thin-layer flow cell also served as a platform for combining DEMS with other analysis methods such as electronic quartz crystal microbalance [29] and attenuated total reflection-infrared spectroscopy [30], but always with stringent requirements on the working electrode. A subsequent modification made it possible to choose working electrodes of various sizes in DEMS, including single-crystals [31], a flexibility also offered by OLEMS, though with a less well-defined geometry for mass transport [24]. Another design of a dual-layer DEMS flow cell focused on the electrode geometry, incorporating a counter electrode parallel to and separated from the working electrode by a membrane, though requiring specialized electrode geometries [32].

Before describing the vacuum inlet system and electrochemical cell behind our new version of EC-MS, we wish to introduce a conceptual framework motivating their design. The three components of a standard quadrupole mass spectrometer (QMS): (1) electron impact ionization (EI), (2) quadrupole mass separation, and (3) detection by a secondary electron multiplier (SEM); all require high vacuum to operate. Above a pressure of approximately $p_v^0 = 10^{-6}$ mbar, mass spectra become less reproducible and signals no longer respond linearly with the amount of analyte [5]. This sets a maximum flux of molecules into the vacuum chamber of the mass spectrometer, dependent on the pumping speed. With the turbo pump used in this paper, which has a pumping speed of $S_{\text{pump}} = 50 \text{ l/s}$, representative of standard turbo pumps for compact vacuum systems, the maximum desired flux into the vacuum chamber is

$$\dot{n}_v^{\text{desired}} = \frac{1}{RT} p_v^0 S_{\text{pump}} \approx 2 [\text{nmol/s}], \quad (1)$$

where R is the gas constant and $T = 298.15 \text{ K}$ is the absolute temperature. Considerations of the SEM and the EI filament longevity also encourage a maximum flux not much higher than this value [33].

In comparison, the production rate of gaseous analytes (hydrogen evolution on platinum, for example) under typical laboratory conditions (current density of $J^{\text{expected}} = -1 \text{ mA/cm}^2$ and electrode area of $A_{\text{el}} = 0.2 \text{ cm}^2$) happens to be

$$\dot{n}_{\text{el}}^{\text{expected}} = \frac{1}{-2\mathcal{F}} J^{\text{expected}} A_{\text{el}} \approx 1 [\text{nmol/s}], \quad (2)$$

where \mathcal{F} is Faraday's constant. In other words, the expected analyte production rate during conveniently-scaled electrochemistry experiments happens to be on the same order of magnitude as the allowable influx to the mass spectrometer of a conveniently-scaled vacuum system. This implies that it should be possible to have 100% *collection efficiency*, i.e. $\eta = 1$, while maintaining an arbitrarily fast time response. Accepting this framework, a clear drawback of both DEMS and OLEMS becomes clear. Since the porous Teflon membranes employed allow a significant amount of solvent evaporation, the analyte will only make up a small portion of the influx to vacuum, and so the influx of analyte to the mass spectrometer must be kept below $\dot{n}_v^{\text{desired}} \sim \dot{n}_{\text{el}}^{\text{expected}}$. This is done either by differential pumping, as in DEMS, lowering the *vacuum collection efficiency*, η_v ; or by limiting the total influx to vacuum, as in OLEMS, lowering the *membrane collection efficiency*, η_m . Either way, the overall collection efficiency $\eta = \eta_m \eta_v$ is lowered. The use of a flow cell also lowers the membrane collection efficiency, as some analyte escapes in the downstream flow [15].

To give a sense of how $\dot{n}_v^{\text{desired}} \sim \dot{n}_{\text{el}}^{\text{expected}}$ compares to the expected magnitude of transient surface phenomena interesting for surface characterization and electrocatalysis, the number of surface atoms in $A_{\text{el}} = 0.2 \text{ cm}^2$ of Pt (111) is about 3×10^{14} , or 0.5 nmol. A monolayer desorption event lasting on the order of a second thus corresponds to a flux on the same order of magnitude as $\dot{n}_v^{\text{desired}} \sim \dot{n}_{\text{el}}^{\text{expected}}$. We refer to the ability to resolve and quantify less than one monolayer of gaseous products on a scale of seconds as *sub-turnover resolution*. In this paper, we present technology enabling sub-turnover resolution for gaseous analytes with 100% collection efficiency, together with full and fast control of dissolved gases at the working electrode. We also present methods for accurate quantification with this system and demonstrate a predictive mass transport model. We anticipate that the technology and concepts presented here will serve as a platform for further improvements in EC-MS, and eventually for in-situ mass spectrometry in other fields as well.

2. Technical

2.1. Membrane chip

Our strategy for achieving a fast and lossless transfer of dissolved gases from the liquid of the test environment to the high vacuum needed for mass spectrometry takes place in two steps. First, the liquid equilibrates across a perforated membrane with a microscopic gas-phase *sampling volume*, allowing any dissolved gases near the membrane to quickly evaporate. Second, gas in this sampling volume is continuously transported through a capillary to the vacuum chamber of the mass spectrometer. The membrane, sampling volume, and capillary are microfabricated into a silicon *membrane chip* using the standard and scalable clean-room techniques of UV lithography, deep reactive ion etching, hydrofluoric acid etching, anodic bonding, and molecular vapor deposition. The membrane is described briefly here. Other membrane chip design parameters as well as its fabrication are described in the supplementary information and in more detail elsewhere [34, 35].

A photograph of the top of the membrane chip is shown in Figure 1a, where the membrane, which has a diameter of 7 mm, shows up as a colorful region due to the diffraction of visible light caused by its microstructure. This structure is shown as a scanning electron microscope image in Figure 1b. Densely spaced holes 2.5 μm in diameter ensure a large surface area to equilibrate with the outside environment while support pillars 50 μm in diameter provide mechanical stability to the membrane, holding it above the 3 μm high sampling volume below. The entire membrane and sampling volume are coated in a hydrophobic self-assembled monolayer (perfluorodecyltrichlorosilane, FDTS) so that an aqueous testing environment immediately above the membrane can be held out of the chip so long as the pressure difference is less than 0.3 bar across the membrane. The sampling volume connects to the mass spectrometer through an outlet in the center which leads to the capillary on the backside of the chip (see Figure S1).

Figure 1c is a schematic diagram of the membrane chip in operation. When the membrane is covered by a liquid testing environment, the sampling volume equilibrates with the liquid, such that the solvent vapor is present in the sampling volume at its vapor pressure, and all dissolved gases and volatile species are (in the ideal approximation) present in the sampling volume at partial pressures proportional to their concentration immediately outside the membrane according to Henry's law of volatility,

$$p_{\text{chip}}^i = K_{\text{H}}^i c^i(0), \quad (3)$$

where K_{H}^i is the Henry's law volatility constant for analyte i (in units $\text{bar}\cdot\text{l}/\text{mol}=\text{bar}/\text{M}$), $c^i(0)$ is its concentration at the membrane, and p_{chip}^i is its partial pressure in the sampling volume of the membrane chip. When the total equilibrium pressure is below ambient pressure, an auxiliary gas is needed to make up the pressure difference and avoid sucking liquid into the chip. This gas, referred to as a *carrier gas* (even though its function is to pressurize the chip, and not to assist in convective transport), is delivered to the rim of the sampling volume, and its composition and pressure are controlled externally (see Figure S1 and S2). Helium is typically used as an inert carrier gas, as its mass spectrum does not overlap with those of other molecules of interest.

The membrane chip is interfaced with the vacuum chamber of the mass spectrometer as indicated in Figure 1d. The capillary is designed such that the total flux to the mass spectrometer, \dot{n}_{v}^0 , is approximately equal to the maximum operation flux described above. The actual flux through the capillary of the membrane chip was determined to be 2.1 nmol/s for air and 2.6 nmol/s for helium by benchmarking against a calibration chip [36],

as described in the supplementary information. The latter value will be assumed below unless otherwise stated:

$$\dot{n}_v^0 = 2.6 \text{ [nmol/s]}. \quad (4)$$

The working principle of the chip is demonstrated in its simplest form in Figure 1e and f. Figure 1e shows a mass spectrum taken with the membrane chip open to air, plotted on a semi-log scale. The main signals include those due to N₂ at $m/z=28$, 14, and 29; O₂ at $m/z=32$, 16, and 34; H₂O at $m/z=18$, 17, 16, 2, and 1; Ar at $m/z=40$ and 20; and CO₂ at $m/z=44$. The signals at select m/z values are monitored as a function of time in Figure 1e. At $t=60$ s, the experimenter exhales on the membrane, resulting in an increased flux of CO₂ which is seen as a spike in the signal at $m/z=44$. At $t=120$ s, the experimenter places a drop of water on the chip, covering the membrane. While the water signal at $m/z=18$ increases, the signals at $m/z=28$, 32, and 40 drop as the dissolved N₂, O₂, and Ar near the membrane are depleted through the chip. As air can no longer enter the sampling volume, carrier gas, in this case He, makes up the pressure difference, seen as a dramatic increase in the signal at $m/z=4$. The drop is removed at 240 s, and air once again displaces He the chip.

2.2. Stagnant thin layer electrochemistry cell

In order to use the membrane chip as a tool for in-situ monitoring of gas-evolving reactions on an electrode surface, we developed the stagnant thin-layer cell illustrated in Figure 2. The cell secures a sample, the *working electrode*, in a position parallel to and close to the membrane. The working electrode, any disk 5 mm in diameter, is mounted in the cell as illustrated in Figure 2a using a PTFE U-cup and spring-loaded disk contacting core available from Pine Research Instruments as the internal hardware for the ChangeDisk RDE tip, making it easy to change working electrodes. Using an optical microscope, the surfaces of the working electrode, u-cup, and cell are brought in-plane to within a few micrometers on the bottom of the cell. The working electrode is electrically contacted from the top of the cell.

The distance between the working electrode and the membrane, referred to as the *working distance*, L , is defined by the thickness of a PTFE gasket with an inner diameter of 12 mm, placed concentric with the membrane and the working electrode, as illustrated in Figure 2b. The docking of the cell to the membrane chip and vacuum system is shown in more detail in Figure S3 of the supplementary information. The volume enclosed by the membrane chip on the bottom, the working electrode and cell on the top, and the gasket on the side, is referred to as the cell *internal volume*. The cell internal volume is contacted by four channels leading outwards to the top of the cell which are used to fill the cell and to make electrolytic contact to external reference and counter electrodes. Two of these channels are shown in the cross-section in Figure 2c.

The portion of the cell internal volume which is between the working electrode and the membrane is referred to as the *working volume*. With a working distance of $L = 100 \mu\text{m}$, used throughout this report, the working volume contains $2.0 \mu\text{l}$ of electrolyte. As illustrated in Figure 2d, gaseous electrochemical reaction products diffuse across this volume from the working electrode to the membrane, where they evaporate to the sampling volume of the chip, and are delivered through the capillary to the mass spectrometer. The membrane extends beyond the working volume by 1 mm in each direction, and the 10:1 aspect ratio of this *edge volume* ensures that a negligible amount of product is lost to lateral diffusion. The working volume and edge volume are simultaneously saturated through the membrane by the carrier gas. Reactant gas can also be introduced through the chip as carrier gas, where it dissolve into the working volume through the membrane and diffuse

to the working electrode. The setup thus symmetrically facilitates fast transport of both reactant and product gases to and from the sample. The full system assembly is shown in Figure S3.

The working distance is an important design parameter for EC-MS experiments involving a stagnant thin-layer cell. The diffusion time from the working electrode to the membrane (on the order of 1-5 s at $L = 100 \mu\text{m}$ for small analyte molecules) scales with the square of the working distance. On the other hand, the electrical resistance from the working electrode to the reference electrode and counter electrode scales inversely with the working distance. We find, in general, that $L = 100 \mu\text{m}$ is a good compromise.

3. Experimental

The membrane chip and stagnant thin layer cell described above, together with a mass spectrometer, potentiostat, and gas manifold, constitute a powerful and versatile tool for studying the reactivity of electrocatalysts. Here, we demonstrate the use of the setup with experiments on a polycrystalline platinum electrode. We chose platinum because it is one of the most studied and well-understood materials in electrocatalysis [37, 38, 39]. This is due to its relatively high stability under a wide range of electrochemical conditions [40, 41] and its high activity for the oxygen reduction reaction (ORR) [42, 43] and hydrogen oxidation reaction (HOR) [44] of hydrogen fuel cells and for the hydrogen evolution reaction (HER) [45, 46] of water electrolyzers.

We show EC-MS data for HER (Reaction 5), the oxygen evolution reaction (OER, Reaction 6), and, by introducing CO through the chip, CO oxidation (COox, Reaction 7).



3.1. Electrochemical reactions on a platinum electrode

The electrochemical experiments presented here involve two types of controlled experimental input: electrode potential and carrier gas composition. There are also two types of observed experimental response: electric current and mass spectrometer signal. All the information in an experiment can be displayed by co-plotting the inputs and outputs on a shared time axis. This type of plot is referred to as an *EC-MS plot*. For convenience, it is separated into a top frame showing calibrated mass spectrometer signals for carrier gas components (left y-axis) and electrochemical products (right y-axis) and a bottom frame showing electrode potential (left y-axis) and electric current (right y-axis).

Figure 3a is an EC-MS plot of an extended electrochemical program on polycrystalline platinum in 1.0 M perchloric acid. Two types of electrical potential input are used: constant-potential steps (chronoamperometry), and potential scanning (cyclic voltammetry) [47]. Fast ramps (200 mV/s) are used between chronoamperometry steps for continuity. While cyclic voltammetry enables easy visualization of redox reactions and is commonly used to characterize electrochemical surfaces, chronoamperometry is essential for studying time-dependent phenomena as scanning techniques convolute the time dependence of the response with the time dependence of the input.

The mass spectrometry data in Figure 3 is calibrated to represent the flux of molecules reaching the mass spectrometer. Because our setup provides 100% collection efficiency for gaseous products, the calibrated signal for products integrates to the amount produced at the electrode. Such absolute quantification is rare in EC-MS, with most contemporary literature reporting raw data, normalized signals, or ratios [13, 17, 15, 18, 25, 27, 23, 26, 28]. Our ability to quantify products is related to the 100% collection efficiency, which makes it straightforward to perform an internal calibration for the mass spectrometer signal corresponding to any gas that can be produced in situ at a known rate. The signals for H_2 at $m/z = 2$, O_2 at $m/z = 32$, and CO_2 at $m/z = 44$ were calibrated during the same experimental run as the measurements shown here by constant-current electrolysis steps according to reactions 5, 6, and 7, respectively, as shown in the supplementary information. When an analyte gas cannot be produced in situ at a known rate, its mass spectrometer signal can instead be calibrated through a calculation of its flux through the capillary [36, 35] (used here for the carrier gases He at $m/z = 4$ and CO at $m/z = 28$) or through extrapolation from internally calibrated signals using a *relative sensitivity factor*, which can

in turn be calculated according the electron impact ionization cross-section and spectrum of the analyte molecule[48] and the transmission function of the mass spectrometer [49]. All of these calibration methods are described in detail in the supporting information.

Starting from the left of Figure 3a, the electrode is held at 0.45 V vs RHE, in the non-reactive “double-layer region”, while the electrolyte is saturated with helium carrier gas. At $t \sim 120$ s, the potential is set to 0.035 V vs RHE for two minutes. Although this is anodic of the equilibrium potential in 1 bar H_2 , H_2 is actively removed through the membrane chip, keeping the partial pressure of H_2 lower than one bar at the electrode, and hydrogen evolution is observed both as a negative (cathodic) current and as a signal at $m/z=2$. Following another period at 0.45 V, at $t \sim 380$ s, the potential is set to 1.750 V vs RHE for two minutes, during which oxygen evolution is observed as positive (anodic) current and signal at $m/z=32$. Unlike HER, which quickly approaches a steady state, OER activity, measured both as current and MS signal, falls quickly during the two minutes constant potential. This has previously been attributed to formation of platinum oxide at the electrode surface [50].

From $t \sim 570$ s to $t \sim 1250$ s, the electrode potential is cycled four complete times between 0.030 V vs RHE and 1.750 V vs RHE at a scan rate of 20 mV/s. During the first two cycles, HER is observed at and around the cathodic and OER at and around the anodic turn, both as current and MS signal. At $t \sim 915$ s, just before the third cathodic turn, the carrier gas is abruptly switched from He to CO. No cathodic current or signal at $m/z=2$ is observed at the cathodic turn at $t \sim 930$ s, indicating that the platinum surface is completely covered in CO, poisoning it for HER. During the subsequent anodic sweep, a spike in current is observed at $t \sim 975$ s, at which point the potential crosses $U \sim 0.85$ V vs RHE, igniting CO oxidation. The signal at $m/z=44$ accordingly increases from the ignition time, reflecting the CO_2 released. OER is still seen at and around the anodic turn. Interestingly, the OER activity is not influenced by the presence of CO.

The potential cycles immediately before and after the switch of carrier gas, indicated by the green and red highlights in Figure 3a, are replotted Figure 3b with the current and $m/z=2$, 32, and 44 signals, projected onto a potential axis, i.e. as *cyclic voltammograms*. The measurements in helium are shown with solid traces, and the measurements in CO with dashed traces. The poisoning of the hydrogen region and lack of OER poisoning described above are clear. It is also clear that there is a small delay in the $m/z=2$ and 32 signals compared to the OER and HER currents, placing the maximum signal after the cathodic and anodic turn, respectively, and that while the $m/z=44$ signal has a steep onset at the ignition of CO oxidation, the signal accumulates thereafter and decays very slowly after CO oxidation ceases at ~ 0.7 V in the cathodic sweep. These effects are due to mass transport of electrochemical products in the working volume, which will be discussed in detail later. The complex behavior of the CO oxidation rate, including ignition at ~ 0.85 V, plateau and gradual decline thereafter, and increase again during the cathodic scan, reflect effects of the state of the platinum surface on CO oxidation [51, 52].

Following the end of cyclic voltammetry in Figure 3a, the electrode potential is set to 1 V vs RHE, just above the ignition of CO oxidation, for two minutes. The current remains relatively constant for the two minutes, while the $m/z=44$ signal approaches steady state much more slowly, and then decays at the same rate after the two-minute period. The mass transport limited CO oxidation current in the setup is

$$j_{mt}^{CO_{ox}} = 2\mathcal{F} \frac{D^{CO}}{L} \frac{p_{chip}^0}{K_H^{CO}} \approx 0.34 \text{ [mA/cm}^2\text{]}, \quad (8)$$

where \mathcal{F} is Faraday’s constant, $D^{CO} = 1.9 \times 10^{-9} \text{ m}^2/\text{s}$ is the diffusion constant of CO in

water [53], $L = 100 \mu\text{m}$ is the working distance between the membrane and the electrode, $p_{\text{chip}}^0 = 1 \text{ bar}$ is the pressure inside the chip, and $K_{\text{H}}^{\text{CO}} = 1100 \text{ bar/M}$ is the Henry's-law volatility constant for CO [54]. The measured current during the constant-potential CO oxidation period is about 0.27 mA/cm^2 , about 20% lower, and slowly declining. This is consistent with the observations by Mayrhofer et al. [51]: While small platinum nanoparticles show a diffusion-limited plateau for potentials just above the ignition of CO oxidation, the rate of CO oxidation on extended polycrystalline platinum surfaces decreases immediately as the surface becomes covered by unreactive oxygen species, with significant deactivation even at 1 V vs RHE.

For many electrochemical experiments, a lasting change of reaction gas is not needed, and instead a short, controlled exposure is advantageous. To this end we use an injection loop on the carrier gas system upstream of the chip (see figure S2), as demonstrated as an EC-MS plot in Figure 3c for a CO stripping experiment on the same polycrystalline platinum electrode. We refer to this technique as *pulse injection*.

Starting from the left of Figure 3c, one complete potential cycle is undertaken between 0.060 and 1.150 V vs RHE with a scan rate of 20 mV/s starting with a cathodic sweep from 0.45 V vs RHE to characterize the state of the electrode surface. Following the cycle, the potential is held at 0.45 V vs RHE while CO is injected from the loop into the carrier gas and flows through the chip from $t \sim 180 \text{ s}$ to $t \sim 240 \text{ s}$. A cathodic CO displacement current is observed, centered around $t \sim 185 \text{ s}$. Following CO exposure, two cycles are carried out, identical to the first cycle. The first cycle shows HER poisoning followed by the oxidation of the adsorbed CO at $t \sim 340 \text{ s}$, and the CO_2 released is immediately observed as a signal $m/z = 44$, which decays slowly thereafter. The last cycle is identical to the cycle before CO exposure, confirming that the electrode surface and setup have returned to their original state free of CO. The small, broad CO_2 signals centered on the anodic turns of the first (before CO exposure) and last cycles are attributed to residual adventitious carbon species on the electrode surface, and not to CO oxidation. The cycle with the CO stripping (green highlight) and the subsequent cycle (red highlight) are plotted as cyclic voltammograms in Figure 3d to better show the difference in current attributed to oxidation of the adsorbed CO.

The integrated CO stripping peak from the cyclic voltammograms corresponds to 370 pmol CO_2 , or about 75% of a monolayer assuming a flat surface, in agreement with literature values [52]. The integrated calibrated mass spectrometer signal for CO_2 , after subtracting the background from oxidation of residual adventitious carbon, is 345 pmol, or about 70% of a monolayer assuming a flat surface, in good agreement with the electrochemistry data. In comparison, the amount of hydrogen produced at $\sim 420 \text{ s}$ in Figure 3 is 24 pmol, corresponding to 5% of a monolayer, i.e., 5% of a catalytic turnover assuming all surface atoms are active.

In addition to the remarkable signal-to-noise ratio for detection of a sub-monolayer of desorbed product, this is, to the best of our knowledge, the fastest full execution of a CO stripping experiment ever reported. By this, we mean the shortest total time required for surface area measurement by CO stripping including a confirmation, by HER poisoning, that the surface has been completely covered by CO; and a confirmation, by prior and subsequent cyclic voltammetry, that the surface has returned to its initial, completely uncovered, state.

4. Modeling

4.1. Preliminary system comparison

As mentioned in the introduction, one of the most important differences between the chip-based inlet system described here and differentially pumped inlet systems used in conventional DEMS is that there is much less solvent evaporation. The water evaporation rate is calculated in the supporting information to be 17 nanoliters per second in DEMS, in approximate agreement with previous calculations [13], and only 1.4 picoliters per second in our chip-based EC-MS.

The 10000 times slower water evaporation is a specific case of the more general phenomenon that the mass transfer coefficient for a molecule across the membrane chip is much smaller than the corresponding mass transfer coefficient across the porous Teflon membrane in DEMS. By mass transfer coefficient we mean the ratio of the flux j_m^i of analyte i across the membrane to its concentration c^i at the membrane:

$$h^i = \frac{j_m^i}{c^i(0)}. \quad (9)$$

The general equations for the mass transfer coefficient h for both systems, derived in the supplementary information, are

$$h_{\text{chip}}^i = K_{\text{H}}^i \frac{\dot{n}_{\text{v}}^0}{p_{\text{chip}}^0 A}. \quad (10)$$

for a chip-based system, where K_{H}^i is the Henry's law volatility constant of species i (from Equation 3 above), \dot{n}_{v}^0 is the total molecular flux through the membrane chip's capillary (Equation 4), $p_{\text{chip}}^0 = 1$ bar is the total pressure inside the chip, and A is the relevant area (the electrode area for products or the membrane area for water); and

$$h_{\text{DEMS}}^i = K_{\text{H}}^i \frac{\phi d_{\text{p}}}{3l_{\text{p}}} \sqrt{\frac{8}{\pi R T M_{\text{mol}}^i}}, \quad (11)$$

Table 1: Molecular properties and response times. Diffusion coefficient [53], Henry's-law volatility constant [54], mass transfer coefficient from Equation 10 or Equation 11, system parameter α from Equation 13, and response time from Equation 14 for selected analytes in our chip-based system (chip) and a differentially pumped system (DEMS).

system	gas	D [m ² s ⁻¹]	K_{H} [bar M ⁻¹]	h [m s ⁻¹]	α	τ [s]
chip	H ₂	4.5×10^{-9}	1300	1.8×10^{-4}	3.8	1.7
	O ₂	2.1×10^{-9}	770	1.0×10^{-4}	4.8	3.3
	CO ₂	1.9×10^{-9}	30	4.0×10^{-6}	0.21	27
DEMS	H ₂	4.5×10^{-9}	1300	3.1	6.8×10^4	1.1
	O ₂	2.1×10^{-9}	770	0.46	2.2×10^4	2.4
	CO ₂	1.9×10^{-9}	30	0.015	7.9×10^2	2.6

for a differentially pumped system, which is governed by Knudsen diffusion [55] through the porous membrane and where ϕ is the porosity (typically 0.5 [15]), l_p is the length of the pores (typically 100 μm), d_p is the pore diameter (typically 20 nm), and M_{mol}^i is the analyte molar mass.

Mass transport of an analyte in the working volume of a stagnant thin-layer system is described by Fick's law of diffusion in the electrolyte and by this mass transfer coefficient at the membrane. A few concepts useful for describing this system can be derived analytically. One simple case is for a sustained constant production rate \dot{n}_{el} of an analyte at the electrode. When steady state is reached, the concentration c is a linear function of the distance y from the membrane:

$$c(y) = \frac{\dot{n}_{\text{el}}}{A_{\text{el}}} \left(\frac{y}{D} + \frac{1}{h} \right), \quad (12)$$

where D is the diffusion constant of the analyte in water (the superscript i has been dropped for convenience). The analyte buildup at the electrode ($y = L$) at steady state thus has two contributions, one of which is due to diffusion in the working volume and one of which is due to evaporation across the membrane. Their ratio,

$$\alpha = \frac{hL}{D}, \quad (13)$$

is a dimensionless parameter describing the relative importance of diffusion and evaporation in the system.

System S17 (supporting information) can be solved analytically using the method of Laplace transformation for the simple case of a step function in $\dot{n}_{\text{el}}(t)$ (see the supporting information for more details). The approximate solution when the system starts at steady state and then the flux from the electrode is turned off is an exponential decay with time constant

$$\tau = \frac{L^2}{2D} + \frac{L}{h}. \quad (14)$$

This time constant is indicated in each of the bottom-row panels of Figure 4. The fact that $\tau^{\text{H}_2} < \tau^{\text{O}_2} \ll \tau^{\text{CO}_2}$ explains the difference in the shapes of the signals for constant-potential H_2 and CO_2 production, i.e., that H_2 reaches steady-state almost immediately and CO_2 has not fully reached steady-state at the end of the two-minute pulse. Mass transfer coefficients h , system parameters α , and characteristic time constants τ are tabulated for select compounds in Table 1.

4.2. Stagnant thin-layer EC-MS

A full mass-transport model for dynamic production of an analyte at the electrode based on the concepts outlined above is described in the supplementary information. To validate the model, four solutions were calculated based on the experimental data in Figure 3. For each of the three constant-potential electrolysis experiments in Figure 3a (HER, OER, and CO oxidation), the concentration of dissolved H_2 , O_2 , or CO_2 , respectively, was calculated according to the model using the appropriate values for h and D . The concentration of dissolved CO_2 was also calculated for the CO stripping experiment in Figure 3c. For the three steady-state experiments we assume 100% Faradaic efficiency for the production of analyte during the 2 minutes of electrolysis (and zero outside of this interval), i.e.,

$$\dot{n}_{\text{el}}(t) = \frac{I(t)}{z\mathcal{F}}, \quad (15)$$

where $I(t)$ is the measured electrical current during the electrolysis period. For the CO stripping experiment, the input is instead based on the assumption that 100% of the difference between cycle 2 and cycle 3 in Figure 3d goes to oxidation of adsorbed CO, i.e., using $\Delta I(t)$ instead of I in Equation 15. In each case the concentration profile can be solved numerically for $c(t, y)$ using the method of lines [56] and the flux through the membrane predicted from the concentration profile according to Equation 9. The predicted flux can be compared to the measured and calibrated mass spectrometer signal.

The modeling is represented in Figure 4, which shows the model input \dot{n}_{el} in the top row, the solution for $c(t, y)$ in the middle row, and the predicted and measured flux co-plotted in the bottom row. The predictions are remarkably good given that no fitted parameters are used in the model.

As the setup and model are refined, we expect that it will become possible to deconvolute mass transport effects from the measured mass spectrometer signals yielding the instantaneous rate of any reaction on the sample with a gaseous product with sub-second resolution.

4.3. Flow EC-MS

The high water evaporation rate in differentially pumped EC-MS necessitates operation in a flow system. To make a relevant comparison, we therefore develop a mass transport model to describe the transport of analyte through a membrane in the collection volume of a flow cell in steady state, as described in the supporting information.

The overall figure of merit is the collection efficiency η , defined as the ratio of the rate analyte reaches the high vacuum of the mass spectrometer at steady state \dot{n}_{v} to the rate at which analyte is produced upstream, \dot{n}_{el} . The collection efficiency is a product of the membrane collection efficiency η_{m} and the vacuum collection efficiency η_{v} ,

$$\eta = \frac{\dot{n}_{\text{v}}}{\dot{n}_{\text{el}}} = \frac{\dot{n}_{\text{m}}}{\dot{n}_{\text{el}}} \frac{\dot{n}_{\text{v}}}{\dot{n}_{\text{m}}} = \eta_{\text{m}} \eta_{\text{v}}. \quad (16)$$

Almost all of the variation between analytes is due the Henry's Law constant of volatility, K_{H} , which determines the mass transfer coefficient through Equations 10 and 11. To give an overview comparing chip-based and differentially pumped EC-MS systems, we therefore plot the collection efficiency η vs K_{H} in Figure 5a. Figures 5b, c, and d show the steady-state concentration profile in the collection volume for H_2 , O_2 , and CO_2 , respectively.

For high-volatility analytes, where η_{m} approaches 1, the chip-based system is much more sensitive than the differentially pumped system, as no analyte is lost to differential pumping ($\eta_{\text{v}} = 1$). In this limit, the ratio of collection efficiencies is the reciprocal of η_{v} , DEMS, i.e.,

$$\left. \frac{\eta_{\text{chip}}}{\eta_{\text{DEMS}}} \right|_{K_{\text{H}} \rightarrow \infty} = \frac{\dot{n}_{\text{m, DEMS}}^{\text{H}_2\text{O}}(T)}{\dot{n}_{\text{v}}^0} \approx 250. \quad (17)$$

For low volatility compounds, the differentially pumped system can be more sensitive due to higher mass transfer coefficients and thus higher values of η_{m} . In the limit that $\eta_{\text{m}} \ll 1$, the ratio of analyte flux to water flux is a constant, and the inefficiency of the chip-based system can be understood as a result of diluting the water vapor and analyte to the chip pressure with carrier gas before delivery to the mass spectrometer.

$$\left. \frac{\eta_{\text{chip}}}{\eta_{\text{DEMS}}} \right|_{K_{\text{H}} \rightarrow 0} = \frac{p_{\text{vap}}^{\text{H}_2\text{O}}(T)}{p_{\text{chip}}^0} \approx 0.03. \quad (18)$$

As a rule of thumb, we propose CO_2 as a transition molecule, defining the volatility at or above which a chip-based system gives a dramatic increase in sensitivity over a differentially pumped system.

4.4. Design considerations

While the above comparison of chip-based and differentially pumped EC-MS is based on a flow model, the same comparison holds qualitatively in a stagnant system, with sensitivity replaced by time response. In a flow system, the time response is fixed according to the flow rate and internal cell volume, while membrane collection efficiency decreases with flow rate and with the solubility of the analyte. In a stagnant system, the membrane collection efficiency is set to unity, i.e., everything is collected if you are willing to wait long enough, but the time response depends on the solubility of the analyte, as shown in Table 1.

The relative advantage of chip-based vs differentially pumped EC-MS thus depends on a number of design parameters including flow vs stagnant, working distance, chip pressure, differential pumping rate, electrolyte flow rate, and temperature. The equations and mass transport models introduced here can help guide the design of the optimal EC-MS setup to study a given electrochemical reaction.

5. Conclusion

This article has demonstrated technical and methodological considerations that are needed in order to measure and interpret minute desorption phenomena during electrochemistry experiments and thereby gain insight into the fundamental reaction mechanisms of electrochemical processes. Laboratory scale electrochemistry experiments often involve desorption phenomena yielding less than 1 nmol of analyte over a few seconds. This makes mass spectrometry an ideal detection method given its instrumental capability of analyzing small amounts of gaseous analyte species with a fast time-response. Mass spectrometry is typically operated with pumping rates which are also on the order of 1 nmol per second. However, coupling a mass spectrometer, with an operational pressure of 10^{-6} mbar directly to an electrochemical experiment is not a trivial task. Conventional methods of designing this interface rely on a membrane to separate the liquid and vacuum environments. This results in a high rate of solvent evaporation lowering sensitivity towards the analyte.

Here, we have presented a unique way of directly coupling electrochemistry and mass spectrometry by means of a microfabricated membrane chip and a stagnant thin-layer cell. The membrane chip acts as an equilibration zone for volatile analyte species between the electrolyte and the MS. The membrane samples the vapor pressure of any volatile analyte into a microscopic sampling volume inside the membrane chip, which is continuously delivered to the mass spectrometer without loss of analyte. By incorporating the membrane chip with a stagnant thin-layer electrochemistry cell, a direct coupling between analyte production at a working electrode and detection at a mass spectrometer was established. Furthermore, the membrane chip enables full control of the dissolved gas atmosphere at the working electrode, allowing either pulsed or steady-state dosing of reactant gases. Modeling of the well-characterized mass transport in this setup makes it possible to compare the anticipated analyte collection rate, based on the current measurement from the electrode, to the measured mass spectrometer signal. As the method is refined, it will become possible to map mass spectrometer measurements directly back to a Faradaic current on the surface of an electrode and thereby deconvolute the signal. While we have focused on electrochemistry studies, it is worth mentioning that the same design paradigm might be equally applicable to e.g. biochemical reaction studies.

It is our hope that the instrumentation presented herein, and the general framework that it represents, will lead to more in-depth studies of sub-monolayer desorption phenomena in the future. This will accelerate advances in electro-catalysis, contributing to the transition to a more sustainable future.

Acknowledgements

Supported by the Villum Foundation V-SUSTAIN grant 9455 to the Villum Center for the Science of Sustainable Fuels and Chemicals.

Methods

The mass spectrometer used in this work is a Pfeiffer QMA 125 with a 90 degree SEM and an open axial beam filament ionizing at 100 eV, which is continuously pumped by a 56 l/s (N₂) Pfeiffer TMP. Electrochemical measurements were made using a Biologic SP-150 potentiostat using the EC-Lab software. An Hg/Hg₂SO₄ reference electrode from Schott Instruments was used, and a gold mesh was used as the counter electrode. The reference and counter electrodes were separated from the cell internal volume by ceramic frits. A 1.0 M HClO₄ electrolyte was prepared by diluting 70% HClO₄ (Merck, Suprapur, 99.99% purity) in deionized water (18.2 MΩ·cm, Millipore). The reference electrode was calibrated against the reversible hydrogen electrode in the same electrolyte saturated with H₂ using two platinum wires as working and reference electrodes. The Ø 5.03 x 3mm polycrystalline platinum disk, from MaTecK, was flame-annealed, cooled under argon atmosphere, and rinsed with Millipore water before use. All glass wear, as well as the stagnant thin-layer cell, were cleaned overnight in a 3:1 mixture of 98 % sulfuric acid and 30% hydrogen peroxide and then thoroughly rinsed with Millipore water before use. Helium and CO are from AGA at 6.0 purity.

For the numerical modelling, the partial differential equations were implemented in python as systems of ordinary differential equations by discretizing in y . A discretization of 30 was used when solving the ordinary differential equations representing the stagnant system, and of 100 when solving for the flow system. The integration was performed using `scipy.integrate.odeint`. All of the data analysis, plotting, and modeling for this article was performed using a homemade python package available at <https://github.com/ScottSoren/>.

Figures

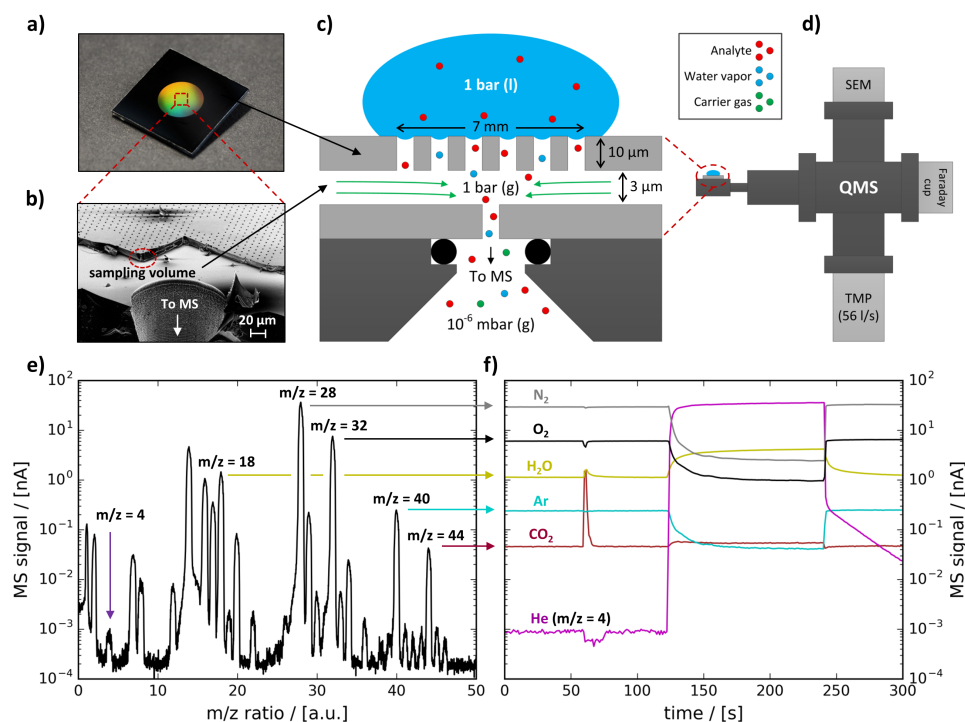


Figure 1: Membrane chip and working principle. **a**, Photograph of the membrane chip. **b**, Scanning electron microscope image revealing internal microstructure of the membrane chip, cut across the middle. The sampling volume is made apparent by the shadow below the membrane, seen clearly in the red circle. **c**, Schematic diagram of the membrane chip under a drop of water (blue) containing dissolved analyte (red). Carrier gas (green) enters the sampling volume bringing the pressure up from the combined equilibrium pressure of water and analyte to atmospheric pressure. Carrier gas, water vapor, and analyte are delivered from the sampling volume through the membrane chip's capillary to the vacuum chamber. **d**, Schematic diagram showing the membrane chip (grey) mounted on a vacuum chamber with a quadrupole mass spectrometer (QMS). **e**, Mass spectrum taken while the membrane chip is uncovered and sampling air. Indicated masses are monitored as a function of time in **f**. The experimenter exhales on the membrane at approximately 60 s, and a drop of water is placed on the membrane at approximately 120 s.

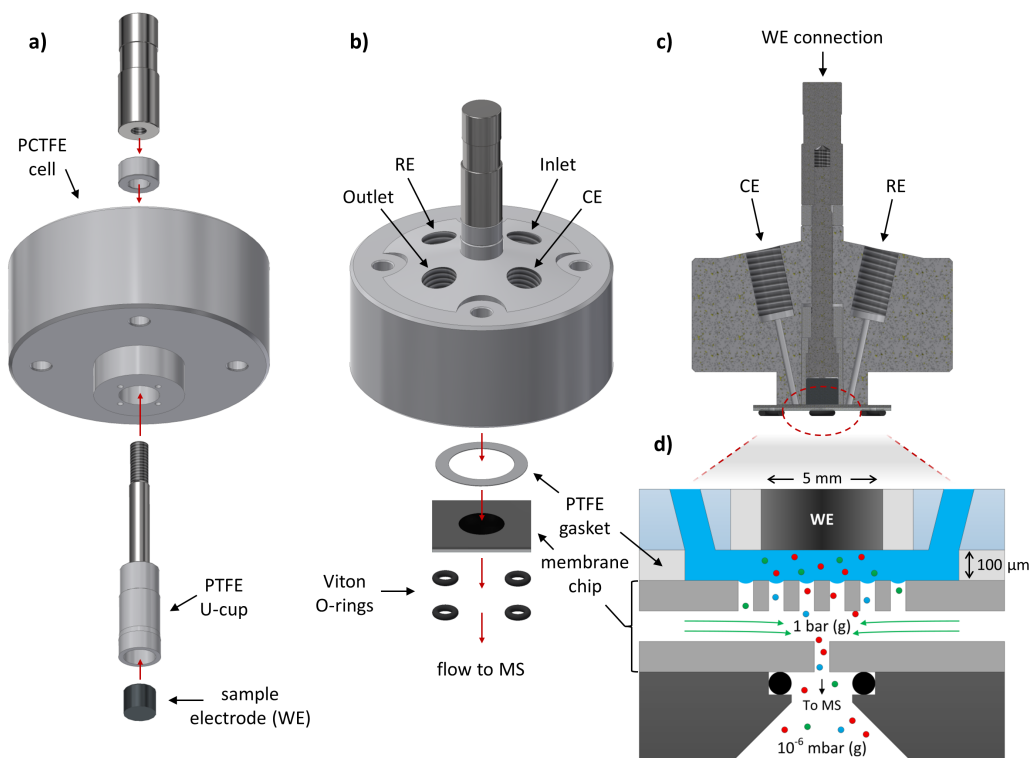


Figure 2: Stagnant thin-layer cell. **a**, Diagram of the cell as seen from below and the cell-electrode assembly. A 5 mm disk electrode is mounted in the cell using a versatile and standardized assembly procedure. **b**, Diagram of the cell-electrode assembly as seen from above and its incorporation with the membrane chip. The working electrode is parallel to the membrane and the distance between them is defined by a PTFE gasket. **c**, Cross section of the cell-electrode assembly and membrane chip showing two of the four liquid channels of the cell. **d**, Schematic diagram of the cell-electrode assembly and membrane chip in operation.

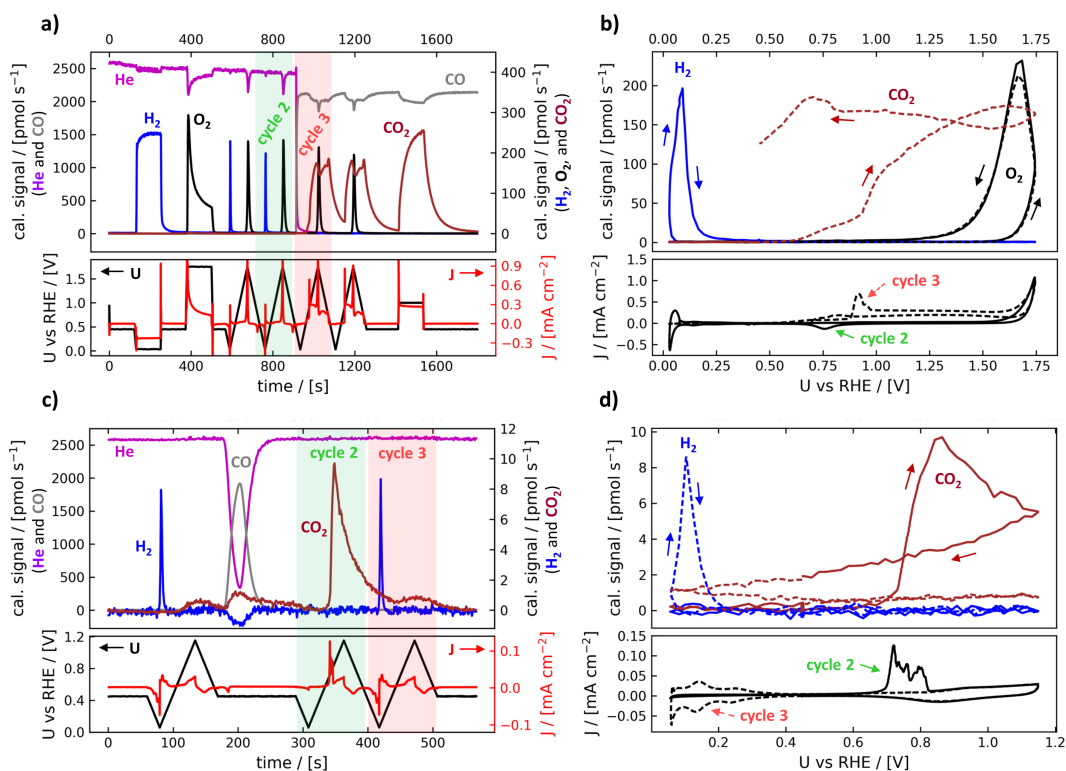


Figure 3: Electrochemistry - mass spectrometry (EC-MS) experiments on platinum. **a**, Demonstration of constant-potential electrolysis at 120 s (hydrogen evolution), 360 s (oxygen evolution), and 1380 s (CO oxidation); cyclic voltammetry (CV) from 600 s to 1200 s; and change of carrier gas from He to CO at 900 s shown as an EC-MS plot. The lower panel shows the electrode potential (black, left axis) and electrical current (red, right axis). The upper panel shows the calibrated mass spectrometer signals for He ($m/z = 4$, magenta) and CO ($m/z = 28$, gray) on the left axis and the signals for H₂ ($m/z = 2$, blue), O₂ ($m/z = 32$, black), and CO₂ ($m/z = 44$, brown) on the right axis. The last CV cycle in He (green highlight) and the first cycle in CO (red highlight) are replotted in **b** as cycle 2 (solid traces) and cycle 3 (dashed traces), respectively. Here the two cycles are co-plotted as cyclic voltammograms, i.e. as a function of the electrode potential. The lower panel shows the electrical current and the upper panel shows the mass spectrometer signals for H₂, O₂, and CO₂. **c**, Demonstration of a gas-pulse injection and subsequent CO stripping experiment shown as an EC-MS plot, with the same coloring as above. A CO displacement current is visible at 185 s. The CV cycle immediately following the CO injection (green highlight) and the subsequent CV cycle (red highlight), are replotted in **d** as cyclic voltammograms.

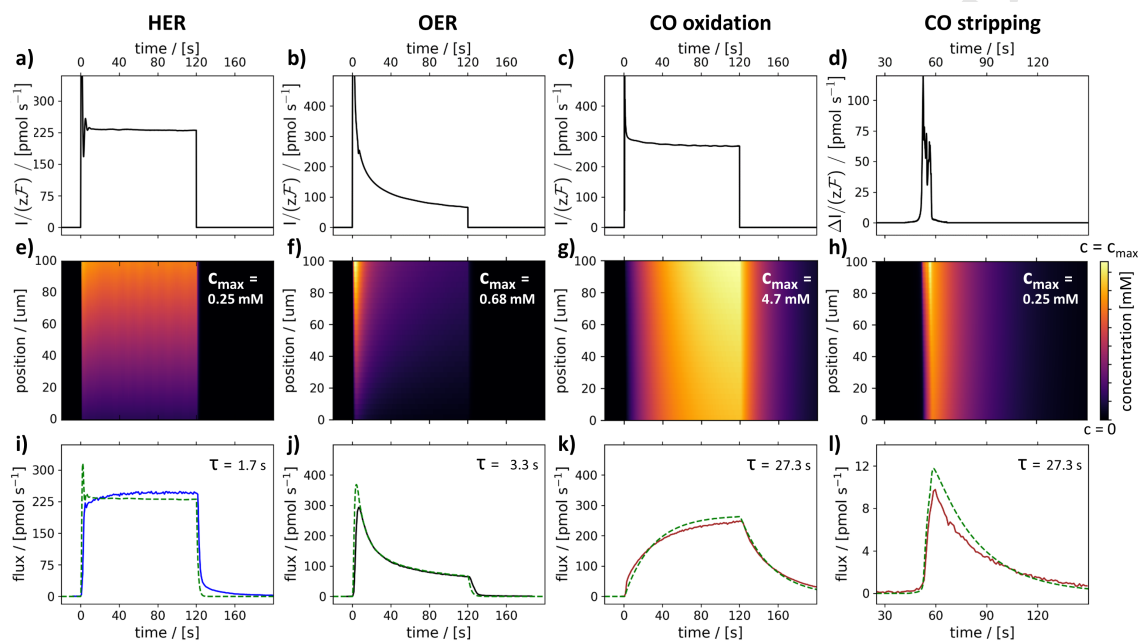


Figure 4: Model validation. **Top row**, Production rate of analyte at electrode assuming 100% Faradaic efficiency for the indicated reaction. **a-c** are based on the electrical current data in Figure 3a during the three constant-potential electrolysis periods, while **d** is based on the difference in electrical current between cycles 2 and 3 in the CO-stripping region in Figure 3d. **Middle row**, Calculated concentration of analyte in the working volume as a function of time (horizontal axis) and distance from the membrane (vertical axis) given the electrode production rate from in the top row. In each panel, concentration varies from 0 (black) to the indicated c_{\max} (bright yellow). **Bottom row**, The flux through the membrane \dot{n}_m , calculated from the concentration profile in the middle row and equation 9, is plotted as a dashed green trace. The relevant calibrated mass spectrometer signal from Figure 3 is co-plotted as a solid trace. The characteristic diffusion-evaporation time calculated by Equation 14 is inset, and the y-axis scale matches that of the top row except for **l**.

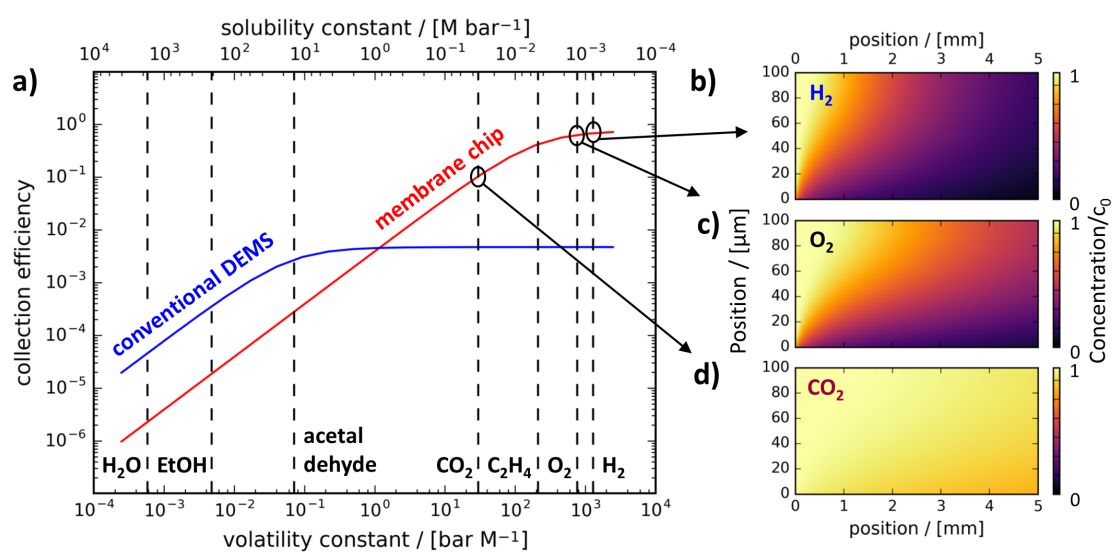


Figure 5: Chip-based vs differentially pumped EC-MS. Model comparison of chip-based and differentially pumped electrochemistry - mass spectrometry in a flow system at steady state. **a**, Overall collection efficiency $\eta = \eta_v \eta_m$ as a function of analyte volatility for chip-based EC-MS (red) and differentially pumped EC-MS (blue) with the volatility of selected analytes indicated. **b-d**, The calculated steady state concentration profiles in the collection volume for H_2 , O_2 , and CO_2 , respectively.

Acknowledgments

Supported by the Villum Foundation V-SUSTAIN grant 9455 to the Villum Center for the Science 208 of Sustainable Fuels and Chemicals.

ACCEPTED MANUSCRIPT

- [1] Intergovernmental Panel on Climate Change. *Climate Change 2014: Synthesis Report*. 2014.
- [2] Nathan S Lewis and Daniel G Nocera. Powering the planet: Chemical challenges in solar energy utilization. *PNAS*, 104(42), 2007.
- [3] Steven Chu, Yi Cui, and Nian Liu. The path towards sustainable energy. *Nature Materials*, 16(1):16–22, 2016.
- [4] Barack Obama. The irreversible momentum of clean energy. *Science*, 6284(January), 2017.
- [5] John R. Yates. *Mass spectrometry: A Textbook*, volume 16. Springer, Heidelberg, second edition, 2000.
- [6] Daniel C. Harris. *Quantitative Chemical Analysis*. W. H. Freeman and Company, New York, eighth edition, 2010.
- [7] Hemma Mistry, Ana Sofia Varela, Stefanie Kühn, Peter Strasser, and Beatriz Roldan Cuenya. Nanostructured electrocatalysts with tunable activity and selectivity. *Nature Reviews Materials*, 1:16009, 2016.
- [8] V. Vojinović, J. M S Cabral, and L. P. Fonseca. Real-time bioprocess monitoring: Part I: In situ sensors. *Sensors and Actuators, B: Chemical*, 114(2):1083–1091, 2006.
- [9] Yu Chie Chen and Pawel L. Urban. Time-resolved mass spectrometry. *TrAC - Trends in Analytical Chemistry*, 44:106–120, 2013.
- [10] George Hoch and Bessel Kok. A mass spectrometer inlet system for sampling gases dissolved in liquid phases. *Arch. Biochem. Biophys.*, 101(1):160–170, apr 1963.
- [11] Erik T. Krogh and Chris G. Gill. Membrane introduction mass spectrometry (MIMS): A versatile tool for direct, real-time chemical measurements. *Journal of Mass Spectrometry*, 49(12):1205–1213, 2014.
- [12] S Bruckenstein and R R Gadde. Use of a porous electrode for in situ mass spectrometric determination of volatile electrode reaction products. *Journal of the American Chemical Society*, 93(3):1966–1967, 1971.
- [13] O Wolter and J Heitbaum. Differential Electrochemical Mass Spectroscopy (DEMS) - A New Method for the Study of Electrode Processes. *Berichte der Bunsengesellschaft für Phys. Chemie*, 6:2–6, 1984.
- [14] Thomas Hartung and Helmut Baltruschat. Differential Electrochemical Mass Spectrometry Using Smooth Electrodes: Adsorption and H/D-Exchange Reactions of Benzene on Pt. *Langmuir*, 6(11):953–957, 1990.
- [15] Helmut Baltruschat. Differential electrochemical mass spectrometry. *Journal of the American Society for Mass Spectrometry*, 15(12):1693–1706, 2004.
- [16] Hatem M.A. Amin and H Baltruschat. How many surface atoms in Co₃O₄ take part in oxygen evolution? Isotope labeling together with differential electrochemical mass spectrometry. *Phys. Chem. Chem. Phys.*, 19:25527–25536, 2017.
- [17] Martin Lanz and Petr Novák. DEMS study of gas evolution at thick graphite electrodes for lithium-ion batteries: the effect of [gamma]-butyrolactone. *Journal of Power Sources*, 102(1-2):277–282, 2001.
- [18] Hongsen Wang, Zenonas Jusys, R. Jürgen Behm, and Héctor D. Abruña. New Insights into the Mechanism and Kinetics of Adsorbed CO Electrooxidation on Platinum: Online Mass Spectrometry and Kinetic Monte Carlo Simulation Studies. *The Journal of Physical Chemistry C*, 116(20):11040–11053, 2012.

- [19] Herbert Oberacher, Florian Pitterl, Robert Erb, and Sabine Plattner. Mass spectrometric methods for monitoring redox processes in electrochemical cells. *Mass Spectrometry Reviews*, 47(12):987–992, 2013.
- [20] Alnald Javier, Jack H Baricuatro, Youn-Geun Kim, and Manuel P Soriaga. Overlayer Au-on-W Near-Surface Alloy for the Selective Electrochemical Reduction of CO₂ to Methanol: Empirical (DEMS) Corroboration of a Computational (DFT) Prediction. *Electrocatalysis*, 6(6):493–497, oct 2015.
- [21] F. J. Vidal-Iglesias, J. Solla-Gullón, J. M. Feliu, H. Baltruschat, and A. Aldaz. DEMS study of ammonia oxidation on platinum basal planes. *Journal of Electroanalytical Chemistry*, 588(2):331–338, 2006.
- [22] J. Souza-Garcia, E. A. Ticianelli, V. Climent, and J. M. Feliu. Mechanistic changes observed in heavy water for nitrate reduction reaction on palladium-modified Pt(hkl) electrodes. *Chemical Science*, 3(10):3063, 2012.
- [23] Youn Geun Kim, Alnald Javier, Jack H. Baricuatro, Daniel Torelli, Kyle D. Cummins, Chu F. Tsang, John C. Hemminger, and Manuel P. Soriaga. Surface reconstruction of pure-Cu single-crystal electrodes under CO-reduction potentials in alkaline solutions: A study by seriatim ECSTM-DEMS. *Journal of Electroanalytical Chemistry*, 780:290–295, 2016.
- [24] A. H. Wonders, T. H M Housmans, V. Rosca, and M. T M Koper. On-line mass spectrometry system for measurements at single-crystal electrodes in hanging meniscus configuration. *Journal of Applied Electrochemistry*, 36(11):1215–1221, 2006.
- [25] Klaas Jan P. Schouten, Elena Pérez Gallent, and Marc T. M. Koper. The influence of pH on the reduction of CO and CO₂ to hydrocarbons on copper electrodes. *Journal of Electroanalytical Chemistry*, 716:53–57, 2013.
- [26] Alexis Grimaud, Oscar Diaz-Morales, Binghong Han, Wesley T. Hong, Yueh-Lin Lee, Livia Giordano, Kelsey A. Stoerzinger, Marc T.M. Koper, and Yang Shao-Horn. Activating lattice oxygen redox reactions in metal oxides to catalyze oxygen evolution. *Nature Chemistry*, (January):1–6, 2016.
- [27] F. Sloan Roberts, Kendra P. Kuhl, and Anders Nilsson. Electroreduction of Carbon Monoxide over a Copper Nanocube Catalyst: Surface Structure and pH Dependence on Selectivity. *ChemCatChem*, 8(6):1119–1124, 2016.
- [28] Cécile S. Le Duff, Matthew J. Lawrence, and Paramaconi Rodriguez. Role of the adsorbed oxygen species in the selective electrochemical reduction of CO₂ to alcohols and carbonyls on copper electrodes. *Angewandte Chemie International Edition*, (10 mL), 2017.
- [29] Zenonas Jusys, Horst Massong, and Helmut Baltruschat. A New Approach for Simultaneous DEMS and EQCM: Electro-oxidation of Adsorbed CO on Pt and Pt-Ru. *Journal of The Electrochemical Society*, 146(3):1093, 1999.
- [30] M. Heinen, Y. X. Chen, Z. Jusys, and R. J. Behm. In situ ATR-FTIRS coupled with on-line DEMS under controlled mass transport conditions-A novel tool for electrocatalytic reaction studies. *Electrochimica Acta*, 52(18):5634–5643, 2007.
- [31] Abd El Aziz A Abd-El-Latif, Jie Xu, Nicky Bogolowski, Peter Königshoven, and Helmut Baltruschat. New Cell for DEMS Applicable to Different Electrode Sizes. *Electrocatalysis*, 3(1):39–47, 2012.
- [32] Ezra L. Clark, Meenesh R. Singh, Youngkook Kwon, and Alexis T. Bell. Differential Electrochemical Mass Spectrometer Cell Design for Online Quantification of Products Produced during Electrochemical Reduction of CO₂. *Analytical Chemistry*, 87(15):8013–8020, 2015.
- [33] *The Vacuum Technology Book*, volume II. Pfeiffer Vacuum GmbH, 2017.

- [34] Daniel B. Trimarco, Thomas Pedersen, Ole Hansen, Ib Chorkendorff, and Peter C K Vesborg. Fast and sensitive method for detecting volatile species in liquids. *Review of Scientific Instruments*, 86(7), 2015.
- [35] Daniel B. Trimarco. *Real-time detection of sub-monolayer desorption phenomena during electrochemical reactions: Instrument development and applications*. Phd thesis, Technical University of Denmark, 2017.
- [36] Toke R. Henriksen, Jakob L. Olsen, Peter Vesborg, Ib Chorkendorff, and Ole Hansen. Highly sensitive silicon microreactor for catalyst testing. *Review of Scientific Instruments*, 80(12), 2009.
- [37] Jie Zheng, Wenchao Sheng, Zhongbin Zhuang, Bingjun Xu, and Yushan Yan. Universal dependence of hydrogen oxidation and evolution reaction activity of platinum-group metals on pH and hydrogen binding energy. *Science advances*, 2(3):e1501602, 2016.
- [38] Yi Fan Huang and Marc T.M. Koper. Electrochemical Stripping of Atomic Oxygen on Single-Crystalline Platinum: Bridging Gas-Phase and Electrochemical Oxidation. *Journal of Physical Chemistry Letters*, 8(6):1152–1156, 2017.
- [39] Vojislav R Stamenkovic, Dusan Strmcnik, Pietro P Lopes, and Nenad M Markovic. Energy and fuels from electrochemical interfaces. *Nat Mater*, 16(1):57–69, 2017.
- [40] Heine A Hansen, Jan Rossmeisl, and Jens K Nørskov. Surface Pourbaix diagrams and oxygen reduction activity of Pt, Ag and Ni(111) surfaces studied by DFT. *Physical Chemistry Chemical Physics*, 10(25):3722–3730, oct 2008.
- [41] Jakob Kibsgaard, Yelena Gorlin, Zhebo Chen, and Thomas F. Jaramillo. Meso-structured platinum thin films: Active and stable electrocatalysts for the oxygen reduction reaction. *Journal of the American Chemical Society*, 134(18):7758–7765, 2012.
- [42] Peter Strasser, Shirlaine Koh, Toyli Anniyev, Jeff Greeley, Karren More, Chengfei Yu, Zengcai Liu, Sarp Kaya, Dennis Nordlund, Hirohito Ogasawara, Michael F. Toney, and Anders Nilsson. Lattice-strain control of the activity in dealloyed core-shell fuel cell catalysts. *Nature Chemistry*, 2(6):454–460, 2010.
- [43] M Li, Mufan Li, Zipeng Zhao, Tao Cheng, Alessandro Fortunelli, Chih-yen Chen, Rong Yu, Lin Gu, Boris Merinov, Zhaoyang Lin, Enbo Zhu, Ted Yu, Qingying Jia, Jinghua Guo, Liang Zhang, William A Goddard Iii, Yu Huang, and Xiangfeng Duan. Ultrafine jagged platinum nanowires enable ultrahigh mass activity for the oxygen reduction reaction. *Science*, 259(1994):In Press, 2016.
- [44] M. Wesselmarm, B. Wickman, C. Lagergren, and G. Lindbergh. Hydrogen oxidation reaction on thin platinum electrodes in the polymer electrolyte fuel cell. *Electrochemistry Communications*, 12(11):1585–1588, 2010.
- [45] E. Kemppainen, A. Bodin, B. Sebok, T. Pedersen, B. Seger, B. Mei, D. Bae, P. C. K. Vesborg, J. Halme, O. Hansen, P. D. Lund, and I. Chorkendorff. Scalability and feasibility of photoelectrochemical H₂ evolution: the ultimate limit of Pt nanoparticle as an HER catalyst. *Energy Environ. Sci.*, 8(10):2991–2999, 2015.
- [46] Jakub Tymoczko, Federico Calle-Vallejo, Wolfgang Schuhmann, and Aliaksandr S. Bandarenka. Making the hydrogen evolution reaction in polymer electrolyte membrane electrolyzers even faster. *Nature Communications*, 7:10990, 2016.
- [47] Allen J Bard and Larry R Faulkner. *Electrochemical methods: fundamentals and application*. Wiley, New York, 2nd edition, 2001.
- [48] S.E. Stein. Mass Spectra. In P.J. Linstrom Mallard and W.G., editors, *NIST Chemistry WebBook, NIST Standard Reference Database Number 69*. National Institute of Standards and Technology, Gaithersburg MD, number 69 edition, 2017.

- [49] D. J. Douglas. Linear Quadrupoles in Mass Spectrometry. *Mass spectrometry reviews*, (28):937–960, 2009.
- [50] Tobias Reier, Mehtap Oezaslan, and Peter Strasser. Electrocatalytic oxygen evolution reaction (OER) on Ru, Ir, and Pt catalysts: A comparative study of nanoparticles and bulk materials. *ACS Catalysis*, 2(8):1765–1772, 2012.
- [51] K. J.J. Mayrhofer, M. Arenz, B. B. Blizanac, V. Stamenkovic, P. N. Ross, and N. M. Markovic. CO surface electrochemistry on Pt-nanoparticles: A selective review. *Electrochimica Acta*, 50(25-26 SPEC. ISS.):5144–5154, 2005.
- [52] Marc T M Koper, Stanley C S Lai, and Enrique Herrero. Mechanisms of the Oxidation of Carbon Monoxide and Small Organic Molecules at Metal Electrodes. *Fuel Cell Catalysis*, pages 159–207, 2009.
- [53] E L Cussler. *Diffusion: Mass Transfer in Fluid Systems (2nd ed.)*. Cambridge University Press, New York, 1997.
- [54] Rolf Sander. Compilation of Henry’s law Constants for Inorganic and Organic Species of Potential Importance in Environmental Chemistry. *Database*, 20(1):107, 1999.
- [55] R B Bird, W E Stewart, and E N Lightfoot. *Transport Phenomena*. John Wiley and Sons, 2 edition, 2007.
- [56] Mark E. Davis. *Numerical methods and modelling for chemical engineers*. 1984.